

1N 34  
139398  
28P

# A Study of Thin Liquid Sheet Flows

Donald L. Chubb and Frederick D. Calfo  
*Lewis Research Center*  
*Cleveland, Ohio*

Marc W. McConley  
*Princeton University*  
*Princeton, New Jersey*

and

Matthew S. McMaster and Abdollah A. Afjeh  
*University of Toledo*  
*Toledo, Ohio*

August, 1993

(NASA-TM-106323) A STUDY OF THIN  
LIQUID SHEET FLOWS (NASA) 28 p

N94-14732

Unclas

G3/34 0189398



— —

# A STUDY OF THIN LIQUID SHEET FLOWS

Donald L. Chubb and Frederick D. Calfo  
National Aeronautics and Space Administration  
Lewis Research Center  
Cleveland, Ohio 44135

Marc W. McConley  
Princeton University  
Princeton, New Jersey 08544

and

Matthew S. McMaster and Abdollah A. Afjeh  
University of Toledo  
Toledo, Ohio 43606

## SUMMARY

This study was a theoretical and experimental investigation of thin liquid sheet flows in vacuum. A sheet flow created by a narrow slit of width,  $W$ , coalesces to a point at a distance,  $L$ , as a result of surface tension forces acting at the sheet edges. As the flow coalesces the fluid accumulates in the sheet edges. The observed triangular shape of the sheet agrees with the calculated triangular result. Experimental results for  $L/W$  as a function of Weber number,  $We$ , agree with the calculated result,  $L/W = \sqrt{8We}$ . The edge cross sectional shape is found to oscillate from elliptic to "cigar" like to "peanut" like and then back to elliptic in the flow direction. A theoretical one-dimensional model was developed that yielded only elliptic solutions for the edge cross section. At the points where the elliptic shapes occur there is agreement between theory and experiment.

## NOMENCLATURE

### Symbols

$A$	area
$c$	wave propagation velocity
$F$	force
$Fr$	Froude number
$g$	gravitational acceleration
$L$	length of sheet
$l$	arc length, slit depth
$p$	pressure
$Q$	volumetric flow rate
$R$	radius of curvature
$r$	$x$ -position at which edge joins main sheet
$s$	sheet edge shape

$U$	dimensionless $x$ -velocity
$u,v,w$	velocity components in Cartesian coordinate system
$W$	slit width
$We$	Weber number
$x,y,z$	Cartesian coordinate system
$\alpha$	shape parameter; ratio of $y$ - $z$ curvature to $x$ - $y$ curvature
$\beta$	parameter related to shape parameter
$\mu$	viscosity
$\xi,\eta,\theta$	dimensionless Cartesian coordinate system
$\rho$	density
$\sigma$	surface tension
$\tau$	sheet thickness
$\psi$	angle between antisymmetric waves and $z$ -axis
<b>Subscripts</b>	
asy	antisymmetric
$c$	edge cross section
$e$	edge
max	maximum value
$o$	initial value
$s$	surface
sy	symmetric
$x,y,z$	partial derivatives with respect to, or components in, Cartesian coordinates
$\xi,\eta,\theta$	partial derivatives with respect to, or components in, dimensionless Cartesian coordinates

## INTRODUCTION

Incompressible, thin sheet flows have been of research interest for many years. Those studies were mainly concerned with the stability of the flow in a surrounding gas. Squire (ref. 1) was the first to carry out a linear, inviscid stability analysis of sheet flow in air and compare the results with experiment. Dombrowski and Fraser (ref. 2) did an experimental study of the disintegration of sheet flows using several viscous liquids. They also detected the formation of holes in their sheet flows. Hagerty and Shea (ref. 3) carried out an inviscid stability analysis and calculated growth rates for the instability. They compared their calculated growth rates with experimental values. Taylor (refs. 4 to 6) studied extensively the stability of thin liquid sheets both theoretically and experimentally. He showed that thin sheets in vacuum are stable. Brown (ref. 7) experimentally investigated thin liquid sheet flows as a method of application of thin films. Clark and Dombrowski (ref. 8) carried out a second order stability analysis for inviscid sheet flows. Lin (ref. 9) introduced viscosity into the linear stability analysis of thin sheet flows in vacuum. Mansour and Chigier (ref. 10) conducted an experimental study of the break up of a sheet flow surrounded by high-speed air. Lin, Lian, and Creighton (ref. 11) did a linear stability

analysis that includes viscosity and a surrounding gas. Rangel and Sirignano (ref. 12) carried out both a linear and nonlinear, inviscid stability analysis that applies for any density ratio between the sheet liquid and the surrounding gas.

Now there is renewed interest in sheet flows because of their possible application as low mass radiating surfaces (refs. 13 and 14). Because of their low mass, near immunity to micrometeoroid damage and simplicity, sheet flows are excellent candidates for a space radiator system. The objective of this study is to investigate the fluid dynamics of sheet flows that are of interest for a space radiator system. Analytical expressions that govern the sheet geometry will be derived and compared to experimental results. Since a space radiator will operate in a vacuum the analysis does not include any drag force on the sheet flow.

Thin sheet flows are dominated by the surface tension forces. As a result of surface tension at the edges of the sheet, a flow that begins with a dimension,  $W$ , perpendicular to the flow direction coalesces to a point at a distance,  $L$ , in the flow direction. The resulting triangular sheet is ideal for a space radiator. In the following analysis results for  $L/W$  scaling and variation of sheet thickness  $\tau$ , that include a constant gravity force in the flow direction, will be derived. Experimental results for  $L/W$  will be compared to the analytical results. Also, analytical results for the edge cross-sectional shape will be calculated and compared with experimental results.

## THEORY

### Sheet Thickness and Sheet Length/Sheet Width Scaling

A sketch of the flow geometry of a thin liquid sheet is shown in figure 1. Surface tension forces at the two edges of the sheet push the edges toward the  $z$ -axis. As a result, as the flow moves in the  $z$ -direction the edge cross-sectional area,  $A_c$ , grows. In order to satisfy mass continuity the edges approach each other and finally meet at the point  $z = L$ .

If sheet flow is to be utilized as a space radiator then the dependence of the sheet length to initial width ratio,  $L/W$ , and sheet thickness,  $\tau$ , on the flow conditions must be known. In this section the  $L/W$  dependence on the Weber number,  $We$ , will be determined. Also, since all experiments have been performed in the Earth's gravity field the  $L/W$  and  $\tau$  dependence on a constant gravity force will be included.

First consider the total force exerted by the surface tension on the edges of the sheet. Consider a cross section of the sheet taken perpendicular to the flow direction as shown in figures 1 and 2. The surface tension pressure is  $\sigma/R_c$ , where  $\sigma$  is the surface tension of the fluid and  $R_c$  is the radius of curvature (ref. 15). Referring to figure 2, the surface tension force on the infinitesimal surface area  $dA = dl \, dz$  is

$$dF = -\frac{\sigma}{R_c} dl \, dz \quad (1)$$

The component of this force in the  $x$ -direction is

$$dF_x = -\frac{\sigma}{R_c} \sin \phi \, dl \, dz = -\frac{\sigma}{R_c} ds \, dz \quad (2)$$

where  $s$  is the cross-section shape and the radius of curvature,  $R_c$ , is given by

$$\frac{1}{R_c} = \frac{\frac{d^2s}{dx^2}}{\left[1 + \left(\frac{ds}{dx}\right)^2\right]^{3/2}} \quad (3)$$

In using (3), any curvature in the  $y$ - $z$  plane is being neglected compared to the curvature in the  $x$ - $y$  plane. This is a good assumption for long ( $L/W > 1$ ) sheet flows.

Substituting (3) in (2) and then integrating over the surface from  $s = 0$  to  $s = \tau/2$  will yield the  $x$ -direction force on the upper half of the sheet edge. Therefore, the total edge force in the  $x$ -direction per unit length in the  $z$ -direction is the following:

$$\frac{dF_x}{dz} = -2 \int_0^{\tau/2} \frac{\sigma s''}{\left[1 + (s')^2\right]^{3/2}} ds \quad (4)$$

where the prime denotes differentiation with respect to  $x$ . Making the substitution  $u = s'$  in (4) yields

$$\frac{dF_x}{dz} = -2\sigma \int_{\infty}^0 \frac{u}{(1 + u^2)^{3/2}} du \quad (5)$$

so that

$$\frac{dF_x}{dz} = 2\sigma \quad (6)$$

The significance of this result is that it is independent of the cross-sectional shape of the sheet. It applies as long as the edge cross section has infinite slope ( $s'' \rightarrow \infty$ ) at the edge ( $x = 0$ ) and zero slope ( $s' = 0$ ) where it joins the constant thickness region ( $x = r$ ).

The  $x$ -direction force given by (6) can be used in the integrated momentum equation for the control volume shown in figure 2. This coordinate system is moving with the edge velocity,  $u_e$ . Therefore, the  $x$ -direction velocity is  $u = -u_e$  at  $x = r$  and  $u = 0$  at  $x = 0$ . The integrated momentum equation combined with (6) yields the following result.

$$\rho \tau u_e^2 = \frac{dF_x}{dz} = 2\sigma \quad (7)$$

Therefore,

$$u_e = \sqrt{\frac{2\sigma}{\rho\tau}} \quad (8)$$

The velocity,  $u_e$ , is the velocity that a free edge of a thin liquid sheet will move regardless of the edge shape. Taylor (ref. 6) derived this result earlier without considering the cross-sectional shape of the edge. This is also the phase velocity,  $c_{asy}$ , of the antisymmetrical wave that can exist on a plane sheet (refs. 5 and 6). Thus for a constant thickness sheet moving with velocity  $w$  in the  $z$ -direction (fig. 1) stationary antisymmetrical waves will make an angle,  $\psi'$ , with the flow direction defined by the following relation (ref. 5)

$$\sin \psi' = \frac{c_{asy}}{w} = \frac{u_e}{w} \quad (9)$$

Also, referring to figure 1,

$$\tan \psi = \frac{u_e}{w} \quad (10)$$

Therefore,  $\sin \psi' = \tan \psi$ . For long sheets ( $L/W > 1$ ),  $\tan \psi \approx \sin \psi$ , so the sheet edge and stationary antisymmetrical waves (lines of constant phase) will be approximately parallel. Experimentally, these waves are observed (fig. 16) as they have also been observed in other experiments (refs. 3, 6, and 10).

Equation (8) gives the sheet edge velocity,  $u_e$ . With this result and the continuity equation, analytical expressions for  $\tau(z)$ ,  $x(z)$ , and  $L/W$  can now be developed. Referring to figure 1(a), at  $z = 0$  the flow will be moving in the  $z$ -direction with initial velocity,  $w_o$ . Eventually, fluid that begins at some position,  $x$ , at  $z = 0$  will be captured by the edge with cross-sectional area  $A_c$ . Therefore, for steady-state conditions the following continuity equation must be satisfied.

$$A_c w_e + \tau x w = \frac{1}{2} \tau_o W w_o \quad (11)$$

In the edge cylinder the  $z$ -direction velocity is  $w_e$ , while in the main sheet the  $z$ -direction velocity is  $w$ . The  $w$  velocity will be determined by the gravitational force, whereas  $w_e$  is determined by the combined gravitational and surface tension forces. Rather than use the complete continuity equation (11), the following simplifying approximation is made. We assume the flow velocity remains entirely in the  $z$ -direction until it reaches the edge. Therefore,

$$\tau x w = \tau_o x w_o \quad (12)$$

Near the slit that creates the sheet flow viscous forces will decelerate the flow. However, Brown (ref. 7) has shown this effect is only important near the slit. Thus, if the gravity force is in the  $z$ -direction (fig. 1) the main sheet flow velocity,  $w$ , is governed by the following equation of motion.

$$\frac{dw}{dt} = w \frac{dw}{dz} = g \quad (13)$$

where  $g$  is the gravitational acceleration. Integration of (13) yields the following.

$$w^2 = w_o^2 + 2gz \quad (14)$$

Also, using the sheet edge velocity in the  $x$ -direction given by (8),

$$\frac{dx}{dt} = w \frac{dx}{dz} = -u_e = -\sqrt{\frac{2\sigma}{\rho\tau}} \quad (15)$$

Now substitute (14) and (12) into (15) to obtain

$$\frac{dx}{dz} = -\sqrt{2We w_o} [w_o^2 + 2gz]^{-1/4} \quad (16)$$

where the Weber number,  $We$ , which is the ratio of the dynamic pressure to the surface tension pressure, is given by

$$We \equiv \frac{\rho w_o^2 \tau_o}{\sigma} \quad (17)$$

Integration of (16) yields the following result for the sheet shape.

$$\frac{2x}{W} = 1 - \frac{2}{3} Fr \sqrt{8/We} \left[ \left( 1 + \frac{2}{Fr} \frac{z}{W} \right)^{3/4} - 1 \right] \quad (18)$$

where the Froude number  $Fr$ , which is the ratio of the kinetic energy to the gravitational energy, is given by

$$Fr \equiv \frac{w_o^2}{gW} \quad (19)$$

When  $x = 0$  the sheet flow will have reached its maximum length,  $z = L$ . Therefore, setting  $x = 0$  in (18) yields the following result for  $L/W$ .

$$\frac{L}{W} = \frac{Fr}{2} \left[ \left( 1 + \frac{3}{2} \frac{1}{Fr} \sqrt{\frac{We}{8}} \right)^{4/3} - 1 \right] \quad (20)$$



The importance of  $We$  in determining  $L/W$  becomes obvious when (20) is expanded for large  $Fr$ . For all the experiments carried out to date  $Fr > 10$ . For the case of no gravity field ( $g = 0$ ),  $Fr \rightarrow \infty$  and (20) yields

$$\left. \frac{L}{W} \right|_{g=0} = \sqrt{\frac{We}{8}} \quad (21)$$

Since  $\sqrt{We} \sim w_o$ , (21) indicates that  $L$  will be a linear function of  $w_o$  for fixed  $W$  and  $\tau_o$ . This was observed in the experiments of Mansour and Chigier (ref. 10) and Chubb and White (ref. 13). Equation (21) for  $L/W$  and the complete expression (20) for several values of  $Fr$  are shown in figure 3. For  $Fr > 20$  there is only a small deviation from the  $Fr \rightarrow \infty$  ( $g = 0$ ) result. Thus for the experimental conditions of this study, (21) can be used to estimate  $L/W$ .

Using the result (21) for  $L/W$  in (18) yields the following equations for the sheet shape in terms of the dimensionless coordinates  $2x/W$  and  $z/L$ .

$$\frac{2x}{W} = 1 - \alpha \left[ \left( 1 + \beta \frac{z}{L} \right)^{3/4} - 1 \right] \quad (22)$$

where

$$\alpha \equiv \frac{2}{3} Fr \sqrt{8/We} \quad (23)$$

and

$$\beta \equiv \left( 1 + \frac{1}{\alpha} \right)^{4/3} - 1 \quad (24)$$

The quantity,  $\alpha$ , can be called the sheet shape parameter since it determines the sheet shape. For most cases of experimental interest  $\alpha \geq 1$ . For  $\alpha \rightarrow \infty$ , (22) becomes

$$\frac{2x}{W} = 1 - \frac{z}{L} \quad \text{for} \quad \alpha \rightarrow \infty \quad (25)$$

Therefore, the sheet is triangular in shape for  $\alpha \gg 1$ . The sheet shape as given by (22) is shown in figure 4(a) for several values of the shape parameter. For  $\alpha \geq 1$  the sheet is essentially triangular in shape. Indeed, this is the result observed experimentally.

Now consider the variation of sheet thickness,  $\tau(z)$ . Combining equations (12), (14), and (20) yields the following result.

$$\frac{\tau}{\tau_o} = \left( 1 + \beta \frac{z}{L} \right)^{-1/2} \quad (26)$$

Similar to  $x(z)$ , the sheet thickness variation  $\tau(z)$  depends only on the shape parameter,  $\alpha$ . Also, for no gravity force,  $\beta = 0$ , and (26) yields  $\tau/\theta_0 = 1$ ; in this case the sheet thickness is a constant. The sheet thickness calculated using (26) for several values of  $\alpha$  is shown in figure 4(b). These theoretical results show that significant thinning of the sheet occurs even for  $\alpha \geq 1$ . However, for  $\alpha \geq 10$  negligible thinning occurs. These results have not been verified experimentally.

### Cross-Sectional Shape of Thin Liquid Sheet

In the preceding section, results for  $L/W$  and  $\tau$  were derived without the need for knowing the cross-sectional shape of the sheet edge. Now the analysis for the cross-sectional shape ( $s(x,z)$  in fig. 2) will be presented. The cross-sectional shape of the sheet edge is important in evaluating the stability of the sheet. The large curvature (small radius of curvature) that exists in the region where the edge joins the sheet ( $x = r$  in fig. 2) can lead to instability. This problem is currently being investigated.

As pointed out in the last section, the effect of the  $z$ -direction gravity force is negligible for the sheet flows of interest. Therefore, only the surface tension force must be considered. In equation (3) of the previous section, the curvature of the sheet in the  $x$ - $z$  plane was neglected so that the surface tension force was confined to the  $x$ - $y$  plane. This is a reasonable assumption for flows of sufficient length ( $L/W > 1$ ). In that case, the cross-sectional shape,  $s(x,z)$ , increases slowly in the  $z$ -direction so that  $s_{xx} \gg s_{zz}$  and only curvature in the  $x$ - $y$  plane is important. The radius of curvature is then given by (3).

For the most general case, however, curvature in the  $x$ - $z$  plane must be included. In the following analysis, the velocity field is assumed to be  $\mathbf{u} = [u(x,z), v(x,y,z), w_0]$ , that is, the flow velocity is constant in the  $z$ -direction and the  $x$ -component of velocity is independent of  $y$ . Assuming irrotational flow, Bernoulli's equation applied at the surface yields:

$$\frac{1}{2}\rho(u_s^2 + v_s^2) - \sigma\left(\frac{1}{R_{xy}} + \frac{1}{R_{yz}}\right) = \frac{\sigma}{R_e} \quad (27)$$

where the subscript  $s$  denotes conditions at the sheet-vacuum boundary. Since the flows of interest are in a vacuum the only pressure appearing in (27) is the surface tension pressure,  $\sigma[1/R_{xy} + 1/R_{yz}]$ , where

$$\frac{1}{R_{xy}} + \frac{1}{R_{yz}} = \frac{\frac{\partial^2 s}{\partial x^2} + \frac{\partial^2 s}{\partial z^2}}{\left[1 + \left(\frac{\partial s}{\partial x}\right)^2 + \left(\frac{\partial s}{\partial z}\right)^2\right]^{3/2}} \quad (28)$$

The right-hand side of (27) is the surface tension pressure that occurs at  $x = 0$  in figure 2 and is a function of  $z$ .

$$\frac{1}{R_e(z)} = \left[\frac{1}{R_{xy}} + \frac{1}{R_{yz}}\right]_{x=0} \quad (29)$$

The sheet surface boundary condition for steady state conditions (A-4) is the following:

$$v_s = u_s \frac{\partial s}{\partial x} + w_o \frac{\partial s}{\partial z} \quad (30)$$

Substituting (30) in (27) we obtain

$$\frac{\rho\tau}{2\sigma} \left[ u_s^2 (1 + s_x^2) + 2u_s w_o s_x s_z + w_o^2 s_z^2 \right] - \tau \frac{s_{xx} + s_{zz}}{(1 + s_x^2 + s_z^2)^{3/2}} = \frac{\tau}{R_e} \quad (31)$$

where the subscripts  $x$  and  $z$  denote partial differentiation. The edge velocity,  $u_e$ , is given by (8) and the Weber number,  $We$ , by (17); substituting these in (31) gives:

$$\left[ \frac{u_s^2}{u_e^2} (1 + s_x^2) + 2 \frac{u_s}{u_e} \sqrt{\frac{We}{2}} s_x s_z + \frac{We}{2} s_z^2 \right] - \tau \frac{s_{xx} + s_{zz}}{(1 + s_x^2 + s_z^2)^{3/2}} + \frac{\tau}{R_e} \quad (32)$$

If the following dimensionless variables are defined,

$$\xi \equiv \frac{x}{\tau/2}, \quad \eta \equiv \frac{s}{\tau/2}, \quad \theta \equiv \frac{z}{\tau/2}, \quad \bar{r} \equiv \frac{r}{\tau/2}, \quad U_s \equiv \frac{u_s}{u_e} \quad (33)$$

then (32) becomes:

$$\eta_{\xi\xi} + \eta_{\theta\theta} = \frac{1}{2} \left[ U_s^2 (1 + \eta_\xi^2) + \sqrt{2We} U_s \eta_\xi \eta_\theta + \left( \frac{We}{2} \right) \eta_\theta^2 - \frac{\tau}{R_e} \right] [1 + \eta_\xi^2 + \eta_\theta^2]^{3/2} \quad (34)$$

An expression for velocity,  $U_s$ , is obtained from the continuity equation derived in Appendix A. By the assumption  $u = u(x, z)$ , we have  $u_s = \bar{u}$ , where  $\bar{u}$  is the average velocity in the  $x$ -direction. Equation (A-7) yields the following:

$$U_s = \frac{1}{\eta} \frac{\partial A / \partial z}{dA_c / dz} \quad (35)$$

where

$$A(x, z) = 2 \int_0^x s \, dx' \quad (A-8)$$

and

$$A_c(z) = 2 \int_0^{r(z)} s \, dx \quad (\text{A-9})$$

is the total cross-sectional area of the sheet edge. Equation (34) is the equation for the sheet edge shape,  $\eta$ , as a function of the dimensionless coordinates  $\xi$  and  $\theta$ . To simplify the solution of (34), the  $\theta$  dependence of the cross-sectional area,  $A$ , is assumed to occur through the edge length dimension,  $r(z)$ . In other words, in rewriting (A-8),

$$A = 2r^2 \int_0^{xr} \left( \frac{s}{r} \right) d\left( \frac{x'}{r} \right) \quad (36)$$

it is assumed that the integral in (36) is independent of  $z$ . In other words, the sheet edge cross-sectional shapes at each  $z$  location are similar. Therefore,

$$U_s = \frac{1}{\eta} \frac{\partial A / \partial z}{dA_c / dz} = \frac{1}{\eta} \frac{\partial \bar{A} / \partial \theta}{d\bar{A}_c / d\theta} = \frac{1}{\eta} \frac{\bar{A}}{\bar{A}_c} \quad (37)$$

where

$$\bar{A} = \frac{2}{\tau^2} A = \int_0^\xi \eta \, d\xi' \quad (38a)$$

and

$$\bar{A}_c = \frac{2}{\tau^2} A_c = \int_0^{\tilde{r}} \eta \, d\xi \quad (38b)$$

Since  $\bar{A}$  depends only on  $\xi$ , equation (37) shows that  $U_s$  is now dependent on  $\theta$  (or  $z$ ) only through  $\bar{A}_c$ .

Substituting (37) into (34) gives the following result for  $\eta(\xi, \theta)$ :

$$\eta_{\xi\xi} + \eta_{\theta\theta} = \frac{1}{2} \left[ \frac{1}{\eta^2} \left( \frac{\bar{A}}{\bar{A}_c} \right)^2 (1 + \eta_\xi^2) + \sqrt{2We} \frac{1}{\eta} \frac{\bar{A}}{\bar{A}_c} \eta_\xi \eta_\theta + \left( \frac{We}{2} \right) \eta_\theta^2 - \frac{\tau}{R_e} \right] [1 + \eta_\xi^2 + \eta_\theta^2]^{3/2} \quad (39)$$

It is desirable to eliminate the  $\theta$  dependence in (39) so that an ordinary differential equation can be obtained. This is done by making the following assumptions. First, it is assumed that in the region of the sheet edge,  $\eta_\xi \gg \eta_\theta$ . This is a good assumption for long sheets ( $L/W > 1$ ) where the edge area,  $A_c$ , grows slowly. Then (39) becomes:

$$\eta_{\xi\xi} + \eta_{\theta\theta} = \frac{1}{2} \left[ \frac{1}{\eta^2} \left( \frac{\bar{A}}{\bar{A}_c} \right)^2 (1 + \eta_\xi^2) - \frac{\tau}{R_e} \right] [1 + \eta_\xi^2]^{3/2} \quad (40)$$

In solving (40), an approximation will be made to treat  $\eta_{\theta\theta}$  as an independent parameter.

As can be seen, by neglecting the  $\eta_\theta$  terms the only dependence on the fluid properties ( $\rho, \sigma$ ), occurs through  $\bar{A}_c$ , which depends on  $W/L$  (eq. (21)). Thus, for a given value of  $\bar{A}_c$  the sheet cross section is the same for all fluids. Solution of equation (40) depends on the parameters  $\bar{A}_c$ ,  $\tau/R_e$ , and  $\eta_{\theta\theta}$ , plus the boundary conditions at  $\xi = 0$  and  $\xi = \bar{r}$ .

$$\text{At } \xi = 0: \eta = 0, \quad \frac{\partial \eta}{\partial \xi} \rightarrow \infty \quad (42a)$$

$$\text{At } \xi = \bar{r}: \eta = 1, \quad \frac{\partial \eta}{\partial \xi} = 0 \quad (42b)$$

The total dimensionless cross-sectional area,  $\bar{A}_c$ , must satisfy the condition  $\bar{A}_c = \bar{A}(\bar{r})$ , so that it is not a free parameter. Instead  $\bar{A}_c$  can be calculated directly from the flow conditions using the continuity equation (11) with the  $Fr \rightarrow \infty$  assumption so that  $w = w_o = w_e$  and  $\tau = \tau_o$ . Therefore, combining equations (11) and (25) yields:

$$A_c = \frac{W \tau_o}{2} \frac{z}{L} \quad (42a)$$

or

$$\bar{A}_c = \frac{W}{\tau_o} \frac{z}{L} \quad (43b)$$

As already mentioned,  $\eta_{\theta\theta}$  is small for the flows of interest ( $L/W > 1$ ). However, the two sets of boundary conditions imply that two independent parameters, namely  $\tau/R_e$  and  $\eta_{\theta\theta}$ , are needed in order to obtain a physically meaningful solution. If  $\eta_{\theta\theta}$  is neglected in (40), it is found numerically that a physically meaningful solution can be obtained for only a unique value of  $\bar{A}_c$ . Since  $\eta_{\theta\theta}$  cannot be neglected, a simplifying assumption is required to reduce (40) to an ordinary differential equation. The simplest assumption is that  $\eta_{\theta\theta}$  is a constant. The procedure for solving (40) using this assumption will now be described, after which it will be shown that this assumption does not yield the true solution. A different assumption will be made, namely  $\eta_{\theta\theta} = \alpha \eta_{\xi\xi}$ . Solutions were investigated using the fourth order Runge-Kutta numerical method (ref. 16).

At  $\xi = 0$ ,  $\eta = 0$ , and  $\eta_\xi$  is infinite, so (40) must be solved analytically near this point. For  $\xi \rightarrow 0$ ,  $\bar{A} \approx \eta_\xi$  (eq. (38a)), so that  $\bar{A}/\eta \rightarrow 0$  and (40) can be approximated by

$$\frac{\eta_{\xi\xi}}{[1 + \eta_\xi^2]^{3/2}} = \frac{-\tau}{2R_e} \quad \text{for } \xi \approx 0 \quad (43)$$

This is the equation for a circle with radius  $2R_e/\tau$  and centered at  $(\xi, \eta) = (R_e/\tau, 0)$ . Therefore, the following are used to calculate  $\eta$  and  $\eta_\xi$  at the first step in the Runge-Kutta integration of (40):

$$\eta \approx \sqrt{\xi \left[ \frac{4R_e}{\tau} - \xi \right]} \quad (44)$$

$$\eta_\xi \approx \frac{2R_e/\tau - \xi}{\eta} \quad (45)$$

The iterative method for solving (40) consists of setting initial values for  $\tau/R_e$ ,  $\eta_{\theta\theta}$ ,  $\bar{A}_c$ , and  $\bar{r}$ , then running the Runge-Kutta routine to get revised values for  $\bar{A}_c$  and  $\bar{r}$ . Eventually,  $\bar{A}_c$  and  $\bar{r}$  converge to a set of values. Since  $\bar{A}_c$  is kept equal to  $\bar{A}$  ( $\bar{r}$ ), and  $\bar{r}$  is defined where  $\eta_\xi = 0$ , the value of  $\eta$  must be checked to see if it equals 1 at  $\bar{r}$ . If not, a new guess for  $\eta_{\theta\theta}$  is made. The process is repeated until a physically meaningful solution is obtained for the value of  $\tau/R_e$  assumed.

This method was applied for several values of  $\tau/R_e$ , and it was determined that a unique solution exists for all values of  $\bar{A}_c$ . The largest value of  $\bar{A}_c$  investigated was 325 200, and the largest  $\bar{A}_c$  which arises in the experiments conducted to date is 2350. Thus it is concluded that a solution to (42) exists for all  $\bar{A}_c$  of interest, and hence for all sheet flow conditions. Figure 5 shows a typical sheet edge shape for  $\bar{A}_c = 1176$ , assuming  $\eta_{\theta\theta}$  is a constant.

Under the assumption that  $\eta_{\theta\theta}$  is a constant, equation (40) breaks down for  $\bar{A}_c < 457$ . Figure 6 shows the two characteristic dimensions of the edge shape solution  $\bar{r}$  and  $\eta_{\max}$  (fig. 5) as a function of  $\bar{A}_c$  ( $= [z/\tau][W/L]$ ). Both quantities appear to follow a trend for  $\bar{A}_c > 457$ , but that trend breaks down for lower areas. Note that  $\bar{A}_c = 457$  is the area at which  $\eta_{\theta\theta} = 0$ .

An examination of the behavior of  $\eta_{\theta\theta}$  as a function of  $\bar{A}_c$  suggests that a constant  $\eta_{\theta\theta}$  is not a good assumption. First, it is known that the curvature in the thin part of the sheet must be zero, since this is essentially a planar region of the sheet. But at the sheet edge, we have assumed  $\eta_{\theta\theta}$  constant. Except for the unique position on the sheet where  $\eta_{\theta\theta} = 0$ , there is a discrepancy. Second, by figure 6, we see that  $\eta_{\theta\theta} < 0$  for small edge areas, but positive curvature would be expected intuitively. The fluid which is just leaving the slit (where  $z/L = 0$  and hence  $\bar{A}_c = 0$ ) is planar, so  $\eta_\theta = 0$ . As the fluid flows down the  $z$ -axis, the edges grow, so we know  $\eta_\theta > 0$ . Therefore, we must have  $\eta_{\theta\theta} > 0$  for at least the lowest range of  $\bar{A}_c$ . Since, from figure 6, the edge shape solutions break down where the  $z$ -curvature is negative, this intuitive violation appears to be related to the breakdown in the theory. Finally, we have assumed the edge shapes to be similar at all stations along the sheet in order to obtain equation (37). This implies  $(\eta_{\max}/\bar{r})$  would be approximately constant, but it is clear from figure 6 that such is not the case. The assumption that  $\eta_{\theta\theta}$  is constant therefore produces an unsatisfactory set of solutions.

The remedy is to make a better assumption on  $\eta_{\theta\theta}$  which avoids these violations. Since surface tension is presumed to act uniformly in all directions, a suitable assumption is to consider the curvature in the  $y$ - $z$  plane to be related to the curvature in the  $x$ - $y$  plane. This is done by setting  $\eta_{\theta\theta} = \alpha \eta_{\xi\xi}$ , where  $\alpha$  is a constant which replaces  $\eta_{\theta\theta}$  as a free parameter. Doing this, (40) becomes

$$\eta_{\xi\xi} = \frac{1}{2(1 + \alpha)} \left[ \frac{1}{\eta^2} \left( \frac{\bar{A}}{\bar{A}_c} \right)^2 (1 + \eta_\xi^2) - \frac{\tau}{R_e} \right] [1 + \eta_\xi^2]^{3/2} \quad (46)$$

Near  $\xi \approx 0$ , this becomes

$$\frac{\eta_{\xi\xi}}{[1 + \eta_\xi^2]^{3/2}} = \frac{-\tau}{2R_e(1 + \alpha)} \quad \text{for } \xi \approx 0 \quad (47)$$

which is the equation for a circle with radius  $2(1 + \alpha)R_e/\tau$  and centered at the point  $(\xi, \eta) = [(1 + \alpha)R_e/\tau, 0]$ . Hence for  $\xi \approx 0$  we have:

$$\eta \approx \sqrt{\xi \left[ \frac{4(1 + \alpha)R_e}{\tau} - \xi \right]} \quad (48)$$

$$\eta_\xi \approx \frac{2(1 + \alpha)R_e/\tau - \xi}{\eta} \quad (49)$$

Again, the Runge-Kutta algorithm reveals that solutions exist for all  $\bar{A}_c$ . Figure 7 shows a typical cross-sectional shape for an  $\bar{A}_c$  of 1231. Note that the edge shape is changed considerably as compared with the shape of figure 5. In figure 8,  $\bar{r}$ ,  $\eta_{\max}$ ,  $\bar{r}\eta_{\max}$ ,  $R_e/\tau$  and  $\alpha$  are plotted as a function of  $\bar{A}_c$ . In figure 8(b) the product  $\bar{r}\eta_{\max}$  is shown as a function of  $\bar{A}_c$ . This linear dependence is the following.

$$\bar{A}_c = 0.731 \bar{r}\eta_{\max} \quad (50)$$

If the shape is purely elliptical then using equation (38b),

$$A_c = \pi s_{\max} \left( \frac{r}{2} \right) = \frac{\tau^2}{2} \bar{A}_c$$

$$\bar{A}_c = \frac{\pi}{4} \bar{r}\eta_{\max} = 0.785 \bar{r}\eta_{\max} \quad (51)$$

Comparing equations (50) and (51) we see that the cross-sectional shape is nearly elliptical.

As figure 8 shows, the assumption that  $\eta_{\theta\theta} = \alpha\eta_{\xi\xi}$  does not result in any of the violations which occurred when  $\eta_{\theta\theta}$  was assumed constant. First,  $\bar{r}$  and  $\eta_{\max}$  are in approximately the same ratio for all  $\bar{A}_c$ , indicating similarity of the sheet edge shape along the flow. This is consistent with the simplifying assumption made about the  $z$  dependence of  $A$ , (eq. (37)). Furthermore, the quantity  $(\bar{r}\eta_{\max})$  is directly proportional to  $\bar{A}_c$ , as expected. Since  $\eta_{\xi\xi} = 0$  on the thin portion of the sheet, we have  $\eta_{\theta\theta} = 0$  in this region the expected result. Finally, over most of the edge we have  $\eta_{\xi\xi} < 0$ . Since for small  $\bar{A}_c$ ,  $\alpha < 0$ , we have  $\eta_{\theta\theta} > 0$  for small edge areas. By the preceding discussion, this is the expected result. Note that at  $\bar{A}_c = 0$ , we must have  $\bar{r} = 0$ , and therefore  $\eta$  is discontinuous at  $\xi = 0$ . Thus the theory cannot predict the shape solution as  $\bar{A}_c \rightarrow 0$ .

The possible existence of oscillatory solutions (i.e., solutions having more than one local minimum for  $\xi > 0$ ) was investigated numerically, and it was determined that such solutions do not exist. Instead,

equation (40) quickly diverges for  $\xi > \bar{r}$ . Occasionally oscillatory solutions were observed, but these occurred only when the assumed value of  $\bar{A}_c$  was much larger than its true value obtained by integrating the area under the shape curve. Also, such solutions were found to diverge when the step size was reduced. Therefore, only one solution, such as that shown in figure 7, appears to exist for each  $\bar{A}_c$ .

## EXPERIMENTAL RESULTS

The objectives of the experimental program are twofold. The first is to verify the scaling relation ( $L/W$  versus  $We$  from (21)). The second is to measure the edge cross section ( $\bar{r}$  and  $\eta_{\max}$ ). In the previous studies of Chubb and White (ref. 13), and Chubb and Calfo (ref. 14), a limited amount of scaling data was obtained. Most of those results were obtained with small slit widths ( $W < 3.5$  cm). For a space radiator system, however, larger slit widths will be used. Therefore, the results reported here are for larger slit widths ( $12.5 \text{ cm} < W < 25 \text{ cm}$ ). All the  $L/W$  versus  $We$  data were taken using low vapor pressure Dow Corning 705 silicone oil at vacuum conditions (less than  $10^{-2}$  torr). However, the edge cross-section results were done in the atmosphere using water as the working fluid. Also, the edge shape data were obtained using small slit widths.

### Experimental $L/W$ Scaling Results

A schematic of the experimental facility used for the  $L/W$  scaling results is shown in figure 9. It consists of a 30-cm inner diameter stainless steel pipe 3.5 m long. The axis of the pipe is aligned with the gravity field. Vacuum conditions exist inside the pipe with the pressure less than  $10^{-2}$  torr. Flow of the Dow Corning 705 silicone oil through the narrow slits is maintained by pressurizing a 40-gal reservoir with nitrogen (nitrogen gas is separated from the oil by a diaphragm to prevent gas entering the oil). The design of the slits is shown in figure 10. A length to slit thickness ratio,  $l/\tau_o = 7$  was chosen to assure that fully developed laminar flow would result.

Four slit widths were used:  $W = 12.5, 18.75, 23.5$ , and  $25$  cm. For  $W = 12.5$  cm, three thicknesses,  $\tau_o = 100, 200$ , and  $300 \mu\text{m}$ , were run. For  $W = 18.75$  cm thicknesses of  $\tau_o = 200$  and  $300 \mu\text{m}$  were run. Thicknesses of  $\tau_o = 100$  and  $200 \mu\text{m}$  were run for  $W = 23.5$  cm, and for the  $W = 25$  cm slit a single thickness of  $\tau_o = 300 \mu\text{m}$  was investigated. The volumetric flow rate,  $Q$ , through these slits was found to satisfy the following relation (ref. 7).

$$Q = \frac{\Delta p \tau_o^3 W}{12\mu l} \quad (52)$$

Where  $\Delta p$  is the pressure drop across the slit and  $\mu$  is the viscosity coefficient. This result was derived for steady flow of liquid between parallel planes by Lamb (ref. 17).

The flow velocity,  $w_o$ , was determined from the measured volumetric flow rate,  $Q$ .

$$w_o = \frac{Q}{W\tau_o} \quad (53)$$

Flow rates were determined by measuring the pressure drop across a calibrated orifice in the supply line to the slits rather than using (52). The velocity,  $w_o$ , was used to calculate the Weber number,  $We$ , using (17). The length,  $L$ , of the sheet was measured with the aid of a video camera mounted on a translating table shown in



figure 9. It is not possible to photograph a complete sheet in this facility. However, figure 11 shows a complete sheet issuing from a small slit ( $W = 3.4$  cm). This photograph is from Chubb and White (ref. 13). Note the triangular shape of the sheet, which agrees with the calculated result (fig. 4(a)).

Scaling results are shown in figure 12 where  $L/W$  is plotted as a function of  $We$ . As can be seen the experimental data points all lie close to the calculated result (21). The properties of Dow Corning 705 oil are temperature-dependent with the density and surface tension given by the following relations that were obtained from the Dow-Corning Company of Midland, Michigan.

$$\rho = 169 - 1.625T \quad [\rho] = \text{kg/m}^3, \quad [T] = K \quad (54a)$$

$$\sigma = 0.08614 - \frac{T}{6502} \quad [\sigma] = \text{N/m}, \quad [T] = K \quad (54b)$$

For the experimental results shown in figure 12,  $T = 98$  °C.

The results in figure 12 are for vacuum conditions. However, experiments in air using water as the sheet fluid yield results that agree with (21). Only a limited range of Weber numbers ( $50 < We < 300$ ) was investigated in the atmospheric experiments. For high velocity flows in air an instability will occur that breaks up the sheet flow.

### Cross-Sectional Shape Experimental Results

The sheet was formed in the atmosphere using water as the working fluid. The photographic technique employed is shown in figure 13. The dashed line represents the line of sight of the camera. A beam splitter and two front faced mirrors were used in order to view both the front and side views of the sheet on the same photograph. The tip of a wire was placed near the sheet edge in order to insure that both images on the photograph were at the same point on the cylinder. Because the sheet edge moves away from the camera in the side view, there was only one place in this view that was in focus. As a result, the camera was set on the tripod with the ability to move forward and back. If the focus on the camera is not adjusted, then any place that is in focus will have the same degree of magnification as any other place that is in focus. Realizing this, it was possible to take a picture of the front view in focus, tape the lens to insure a constant focal length, and move the camera forwards and back in order to get a number of points along the edge view of the sheet in focus.

The camera used was a Nikon F4 equipped with a fully extended bellows and a 200-mm Nikon lens, with a +2 diopter close-up lens. Kodak TMAX 400 black and white film was used. Three different slit thicknesses (50, 80, and 100  $\mu\text{m}$ ) were used, and one set of data was collected from each. All the slits were 3.4 cm wide.

Once a full, steady liquid sheet was formed the length of the sheet was measured. The wire tip was placed near the edge, close to the top of the sheet and the distance from the tip of the wire to the top of the sheet was measured. The camera and mirrors were placed so the wire would have the same length in each view near the bottom of the frame. Two pictures were taken showing both views, and the lens was fixed in place to ensure an equal degree of magnification for each picture. Two pictures were then taken showing just the front view for greater clarity. Four or five pictures were taken showing different points in the edge view in focus. This procedure yielded four or five data points along approximately 1 in. of the edge.

At this point, a picture of a millimeter scale was taken in order to determine the degree of magnification of the pictures after developing. Then the wire was moved down allowing the top of the next set of photographs to be at the same point as the bottom of the previous set. The height of the wire tip was measured again and the next set of pictures taken. A picture of the millimeter scale was taken after each set of pictures to check that the degree of magnification was not changing. The length of the sheet was periodically measured to check that the length of the sheet was staying constant.

Enlarged photographs were made for taking the  $\bar{r}$  and  $\eta_{\max}$  measurements. The pictures of the scale were measured with a millimeter scale to determine the degree of magnification. Knowing the position of the wire tip, the blown-up photograph of the scale could be used to determine the height of the point that appeared to be in focus in each of the edge shots. The cylinder widths and thicknesses were measured to a resolution of a 64th of an inch.

Knowing the dimensions of the slit, the total length of the sheet, and the height at which the data points were taken, the dimensionless cross-sectional area of the edge,  $\bar{A}_c$ , could be calculated using (42b). Knowing the degree of magnification and the dimensions of the slit,  $\eta_{\max}$  and  $\bar{r}$  could be calculated using (33). These data and the theoretical predictions are shown in figure 14.

Figure 14 reveals a very interesting phenomenon. The edge appears to be oscillating in the flow direction,  $z$ . The edge quickly flattens out and then reforms in its basically elliptic shape. When the edge is in its elliptic shape it is in good agreement with the theoretical predictions. The details of this cycle are shown in figures 15 and 16. Figure 15 shows a cross section of the edge in the  $x$ - $y$  plane; figure 16 is a photograph taken, as described in figure 13, of edge and plan views of the sheet. Figure 16(a) is a photograph of the edge very near the top of the sheet, where the edge takes on a basically elliptic shape. Figure 16(b) shows the section of the edge just below that shown in figure 16(a), where the edge goes through the flattening out and reforming process. At the bottom of each photograph the front and side views of the wire tip can be seen. Also notice the antisymmetrical waves (with lines of constant phase running parallel to the sheet edge) that appear next to the edge in the plan view in figure 16.

The edge begins in its nearly elliptic shape, shown in figure 16(a). Due to the high curvature where the edge connects to the sheet, the edge quickly flattens out to a "cigar" like shape, shown near the top of figure 16(b). This appears in figure 14 as an increase in  $\bar{r}$  and a decrease in  $\eta_{\max}$ . Instead of simply regaining its elliptic shape, the edge goes through a rebuilding process where the edge has a "peanut" like shape. As the area of the edge increases,  $\eta_{\max}$  increases first on the inside of the previous edge. This can be seen best a third of the way down the edge view of figure 16(b), where the inner part of the edge can be seen behind the outer part of the edge. It is not clear whether the edge necks down between these two parts. This inner part of the edge grows and engulfs the outer part to return to its elliptic shape. This appears in figure 14 as an increase in  $\eta_{\max}$  and a decrease in  $\bar{r}$ . This is most noticeable in the 100- $\mu$ m slit.

As discussed earlier, the only edge shape solutions obtained analytically are elliptic (fig. 7). No "peanut" or "cigar" like shapes, which were observed experimentally (fig. 15), were calculated. Assumptions were made about the  $z$ -direction derivatives,  $\eta_\theta$  and  $\eta_{\theta\theta}$ , in order to reduce the two-dimensional problem (34) to a one-dimensional problem (46). Also, in (36) the edge shapes were assumed similar at each  $z$ -location in order to reduce the problem to one dimension. However, the "peanut" and "cigar" shapes observed indicate that the assumptions  $\eta_\theta \ll \eta_{\bar{r}}$ ,  $\eta_{\theta\theta} = \alpha \eta_{\bar{r}\bar{r}}$ , and similarity of the edge cylinders do not apply in those cases. Solutions like the experimental "cigar" and "peanut" edge shapes require a three-dimensional formulation.

## SUMMARY

This study was a theoretical and experimental investigation of the fluid mechanics of thin liquid sheet flows in vacuum. Surface tension forces at the edges of the sheet result in a triangular shape for the sheet of width,  $W$ , and height,  $L$ . The flow coalesces to a point at the distance,  $L$ , with the fluid being accumulated at the sheet edges. Theoretical results that include the gravity force acting in the flow direction yield a triangular shape for the sheet. Extensive experimental data for  $L/W$  as a function of Weber number,  $We$ , agree with the theoretical result for no gravity force,  $L/W = \sqrt{We}/8$ . Theoretical results show that for Froude numbers of experimental interest the gravity force has negligible effect on  $L/W$ .

Solutions for the edge cross-sectional shape were obtained from a one-dimensional model that includes only the surface tension forces. All calculated edge cylinder solutions are elliptic in shape. However, experimentally it was found that the edges oscillate in the flow direction between elliptic, "cigar" and "peanut" like cross-sectional shapes. There is agreement between the theory and experiment at the points where the elliptic shapes occur. To account for "cigar" and "peanut" like shapes requires the theoretical model to be extended to three dimensions.

## Acknowledgment

There are several people who are not authors that deserve recognition. Jose Ayala constructed the variable slit and Larry Cousino set up the experiment. Chris Van Campen devised the photographic technique used to measure the end cylinders. David Jacqmin supplied a simplified approach for obtaining the sheet shape solution (22). Finally, James Zakany aided in the experimental program.

## APPENDIX A

### Continuity Equation Solution

The continuity equation for steady-state incompressible flow is the following.

$$\frac{\partial u}{\partial x} + \frac{\partial v}{\partial y} + \frac{\partial w}{\partial z} = 0 \quad (\text{A-1})$$

where  $u$ ,  $v$ , and  $w$  are respectively the  $x$ -,  $y$ -, and  $z$ -direction velocities. Referring to figure 2, if (A-1) is integrated from  $0 \leq y \leq s(x,z)$  then (A-1) becomes the following.

$$\frac{\partial}{\partial x}(s\bar{u}) + \frac{\partial}{\partial z}(s\bar{w}) + v_s - u_s \frac{\partial s}{\partial x} - w_s \frac{\partial s}{\partial z} = 0 \quad (\text{A-2})$$

where  $\bar{u}$  and  $\bar{w}$  are average velocities defined as follows:

$$\bar{u} = \frac{1}{s} \int_0^s u \, dy \quad \bar{w} = \frac{1}{s} \int_0^s w \, dy \quad (\text{A-3})$$

and since the flow is symmetric about the  $x$ -axis,  $v(y=0) = 0$ .

At the sheet surface the fluid  $y$ -direction velocity,  $v_s$ , must equal the surface speed,  $ds/dt$ . Therefore, for steady-state conditions,

$$\frac{ds}{dt} = u_s \frac{\partial s}{\partial x} + w_s \frac{\partial s}{\partial z} = v_s \quad (\text{A-4})$$

Using (A-4) in (A-2) yields the following

$$\frac{\partial(s\bar{u})}{\partial x} + \frac{\partial(s\bar{w})}{\partial z} = 0 \quad (\text{A-5})$$

Since the gravity force and surface tension force (curvature in the  $y$ - $z$  plane) in the  $z$ -direction are being neglected,  $\bar{w}_z \ll \bar{u}_x$ . Therefore,

$$\frac{\partial(s\bar{u})}{\partial x} = -\bar{w} \frac{\partial s}{\partial z} \quad (\text{A-6})$$

Beginning at  $x = 0$  where  $s = 0$ , and  $\bar{u} = 0$ , integrate with respect to  $x$  to obtain:

$$s\bar{u} = -\frac{1}{2} \bar{w} \frac{\partial s}{\partial z} \quad (\text{A-7})$$

where

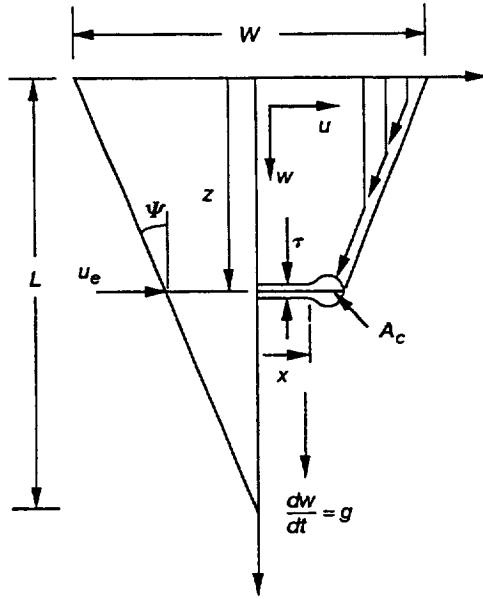
$$A(x,z) = 2 \int_0^x s(x',z) dx' \quad (\text{A-8})$$

is the sheet edge cross-sectional area for  $0 \leq x' \leq x$  (fig. 2). When  $x = r(z)$ , we have  $A = A_c$  and  $s\bar{u} = -(\tau/2)u_e$ , where  $A_c$  is the total sheet edge cross-sectional area. Therefore,

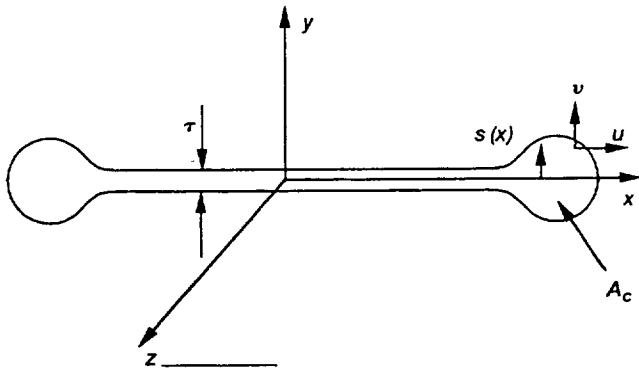
$$A_c(z) = 2 \int_0^{r(z)} s(x',z) dx' \quad (\text{A-9})$$

## REFERENCES

1. Squire, H.B., *Investigation of the Instability of a Moving Liquid Film*, British Journal of Applied Physics, Vol. 4, 1953, pp. 167–169.
2. Dombrowski, N., and Fraser, R.P., *Photographic Investigation into the Disintegration of Liquid Sheets*, Philosophical Transactions, Vol. A247, 1954, pp. 101–130.
3. Hagerty, W.W., and Shea, J.F., *A Study of the Stability of Plane Fluid Sheets*, Journal of Applied Mechanics, Vol. 22, 1955, pp. 509–514.
4. Taylor, G.I., *The Dynamics of Thin Sheets of Fluid, I. Water Bells*, Proceedings of the Royal Society of London, Vol. A253, 1959, pp. 289–295.
5. Taylor, G.I., *The Dynamics of Thin Sheets of Fluid, II. Waves on Fluid Sheets*, Proceedings of the Royal Society of London, Vol. A253, 1959, pp. 296–312.
6. Taylor, G.I., *The Dynamics of Thin Sheets of Fluid, III. Disintegration of Fluid Sheets*, Proceedings of the Royal Society of London, Vol. A253, 1959, pp. 313–321.
7. Brown, D.R., *A Study of the Behavior of a Thin Sheet of Moving Liquid*, Journal of Fluid Mechanics, Vol. 10, 1961, pp. 297–305.
8. Clark, C.J., and Dombrowski, N., *Aerodynamic Instability and Disintegration of Inviscid Liquid Sheets*, Proceedings of the Royal Society of London, Vol. A329, 1972, pp. 467–478.
9. Lin, S.P., *Stability of a Viscous Liquid Curtain*, Journal of Fluid Mechanics, Vol. 104, 1981, pp. 111–118.
10. Mansour, A., and Chigier, *Disintegration of Liquid Sheets*, Physics of Fluids, Vol. A2, No. 5, 1990, pp. 706–719.
11. Lin, S.P., Lian, Z.W., and Creighton B.J., *Absolute and Convective Instability of a Liquid Sheet*, Journal of Fluid Mechanics, Vol. 220, 1990, pp. 673–689.
12. Rangel, R.H., and Sirignano, W.A., *The Linear and Nonlinear Shear Instability of a Fluid Sheet*, Physics of Fluids, Vol. A3, No. 10, 1991, pp. 2392–2400.
13. Chubb, D.L., and White, K.A., *Liquid Sheet Radiator*, AIAA Paper 87–1525, 1987. (Also, NASA TM–89841.)
14. Chubb, D.L., and Calfo F.D., *Scaling Results for the Liquid Sheet Radiator*, Proceedings of 24th IECEC, Vol. 1, Washington, DC, 1989, pp. 45–50. (Also, NASA TM–102100.)
15. Batchelor, G.K., *An Introduction to Fluid Dynamics*, Cambridge University Press, New York, 1967, pp. 60–64.
16. Press, W.H., Flannery, B.P., Teukolsky, S.A., and Vetterling, W.T., *Numerical Recipes, The Art of Scientific Computing*, Cambridge University Press, New York, 1986, pp. 550–554.
17. Lamb H., *Hydrodynamics*, 6th ed. Cambridge University Press, New York, 1932, p. 582.



(a) Top view.



(b) Cross section view.

Figure 1.—Schematic of thin liquid sheet flow.

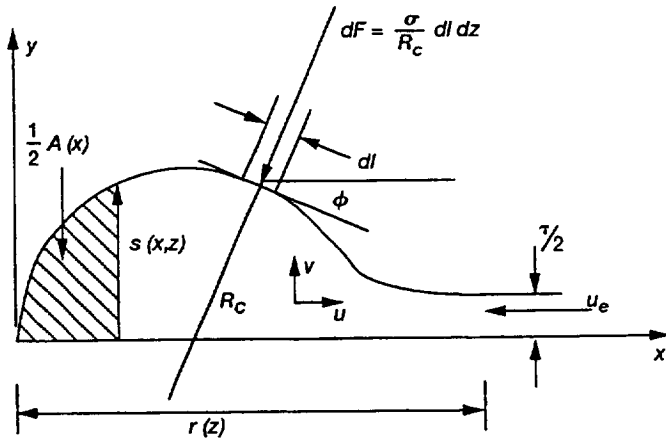


Figure 2.—Sheet edge control volume in coordinate system moving with edge velocity,  $u_e$ .

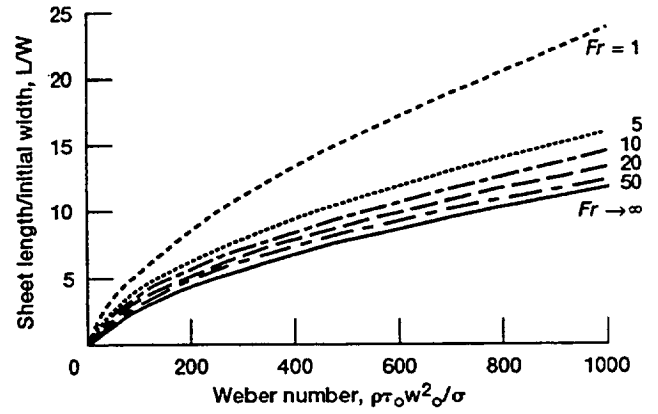
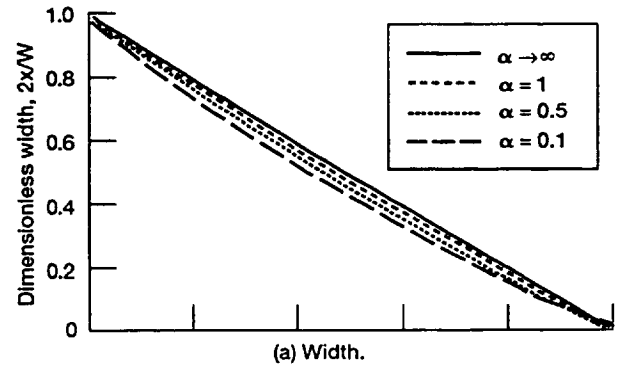
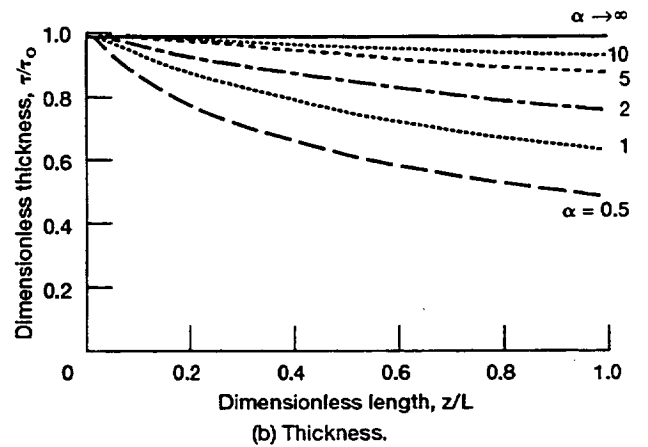


Figure 3.—Sheet length to initial width ratio.



(a) Width.



(b) Thickness.

Figure 4.—Sheet shape as a function of sheet shape parameter,  $\alpha$ .

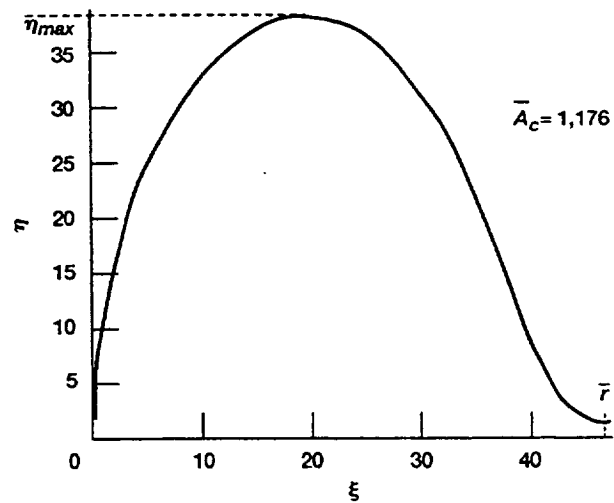


Figure 5.—Sample calculated cross section. Assumes  $z$ -curvature constant.

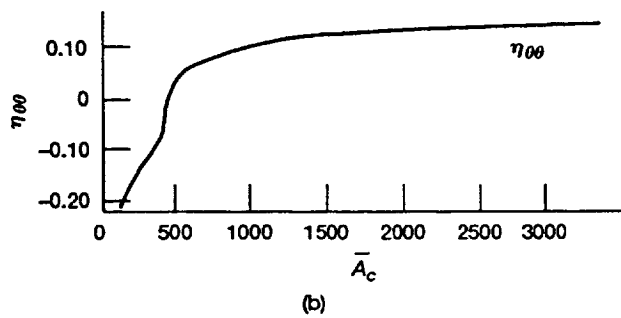
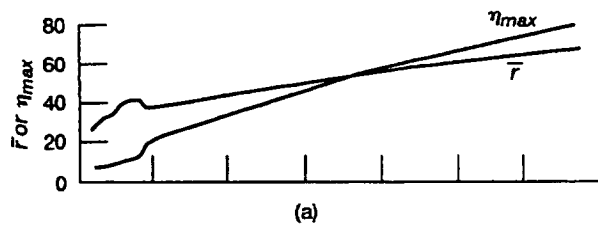


Figure 6.—Dependence of sheet edge parameters on edge cross-sectional area. Assumes  $y$ - $z$ -curvature constant.

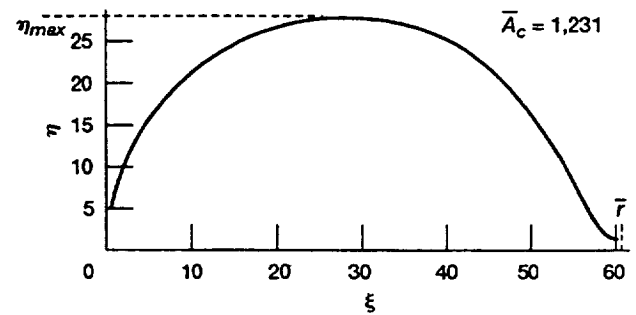


Figure 7.—Sample calculated cross section. Assumes  $y$ - $z$  curvature proportional to  $x$ - $y$  curvature.



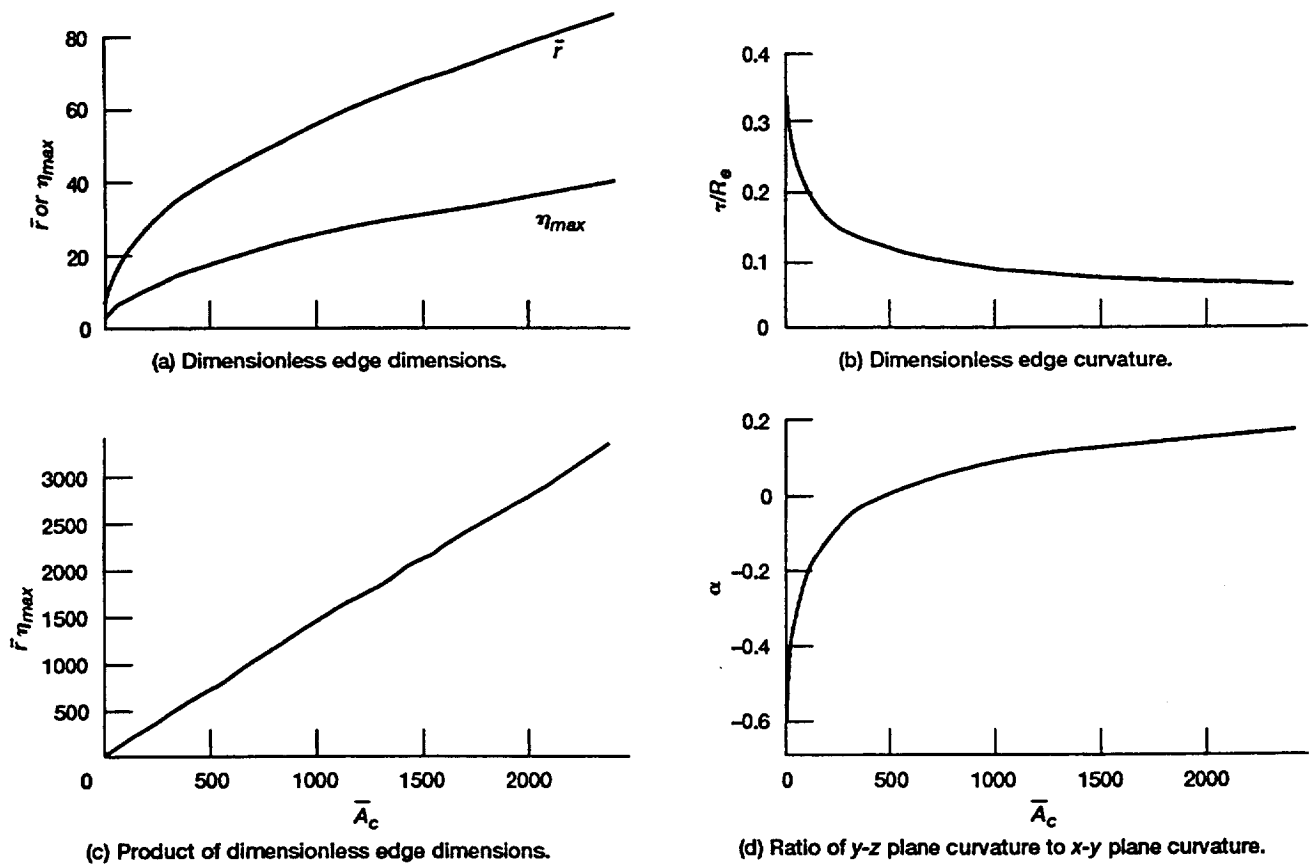


Figure 8.—Dependence of sheet edge parameters on edge cross-sectional area. Assumes y-z curvature proportional to x-y curvature.

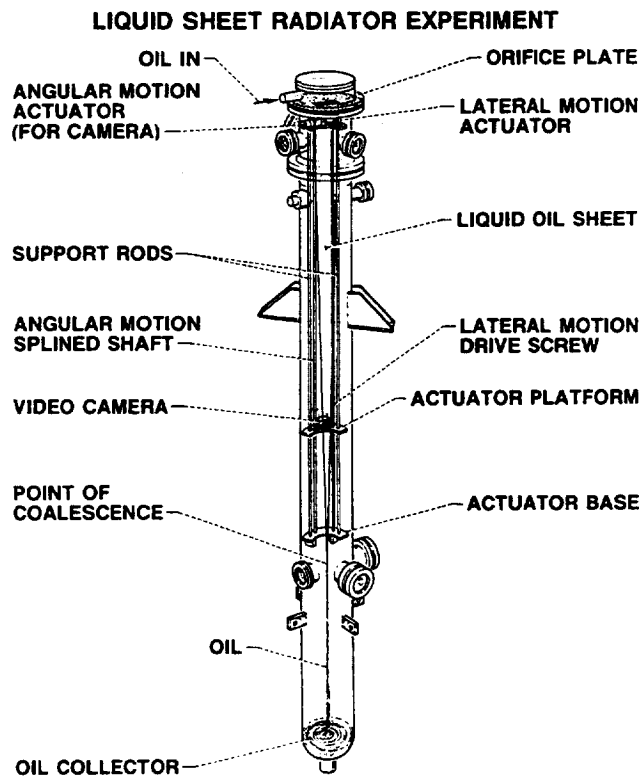


Figure 9.—Schematic of experimental facility for determining  $L/W$  scaling.

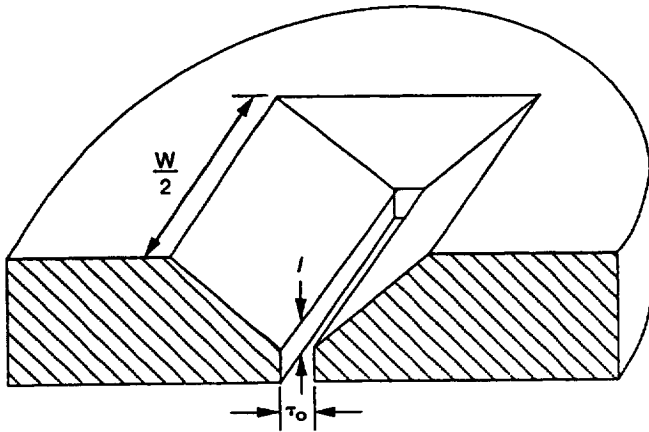


Figure 10.—Typical slit plate for producing sheet flow.

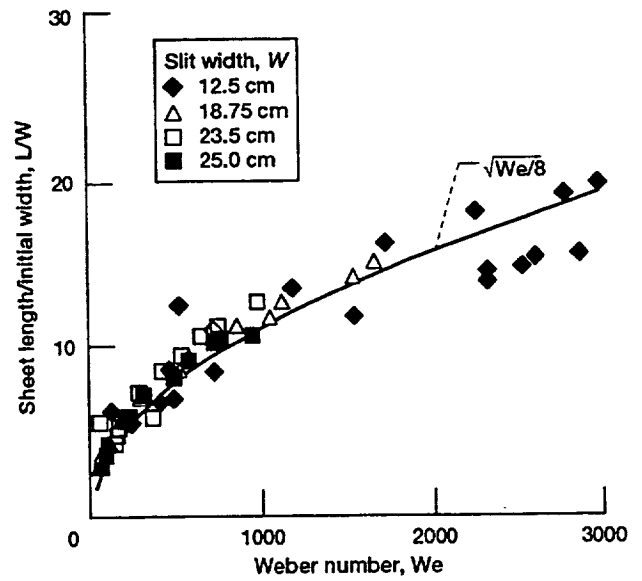


Figure 12.—Comparison of theoretical and experimental sheet scaling.

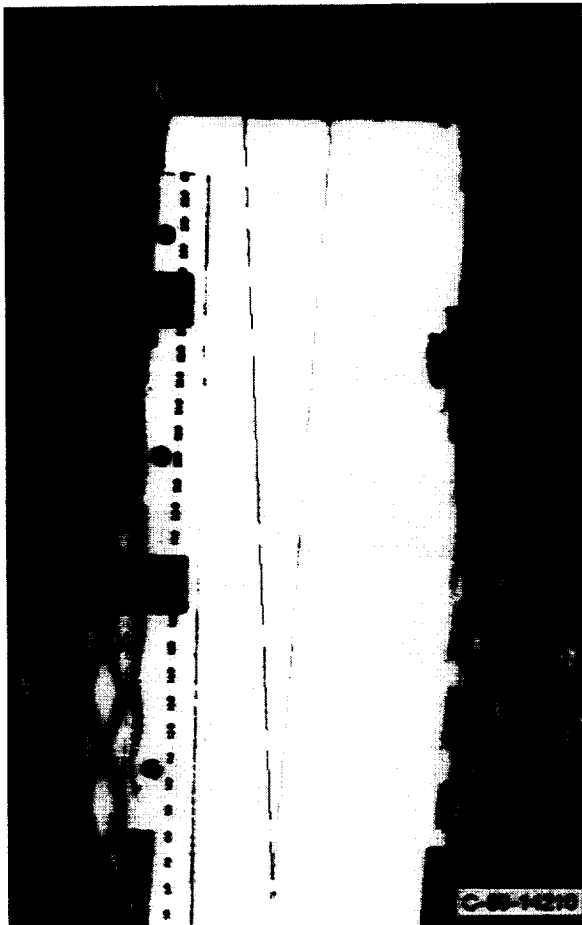


Figure 11.—Sheet flow of Dow-Corning 705 oil from a 3.4 cm wide slit.  $\tau_o = 109 \mu\text{m}$ ,  $l/\tau_o = 3.4$ ,  $L/W = 9.6$ ,  $w_o = 11.1 \text{ m/s}$ .

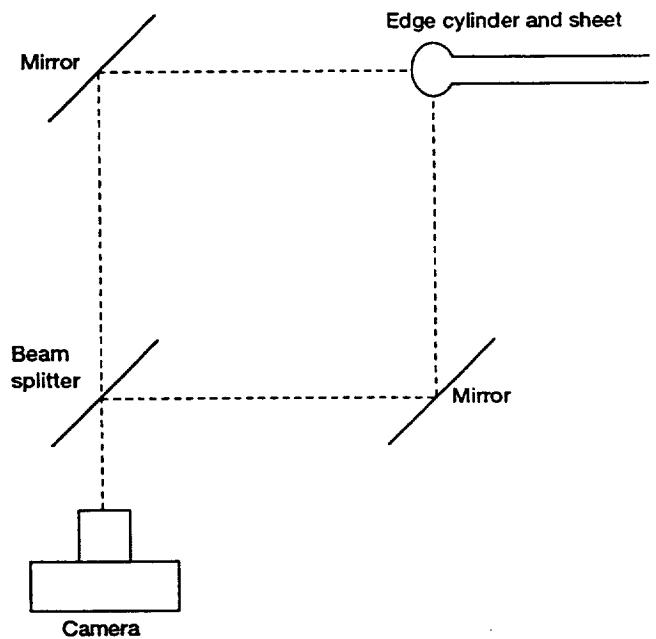


Figure 13.—Photographic set up for measuring end cross section.

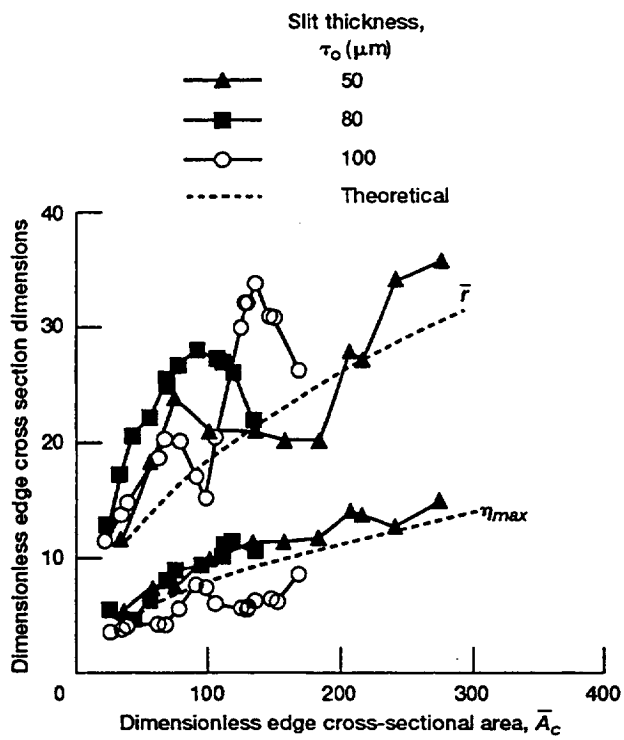
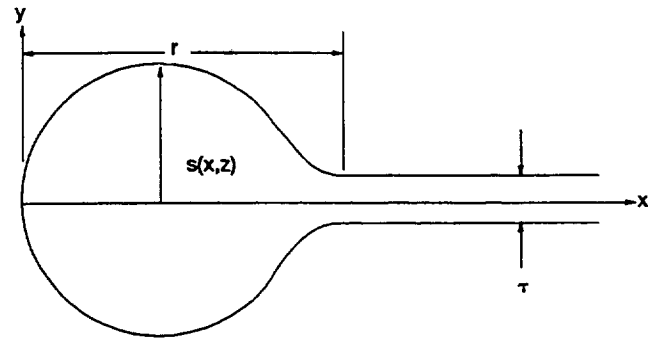
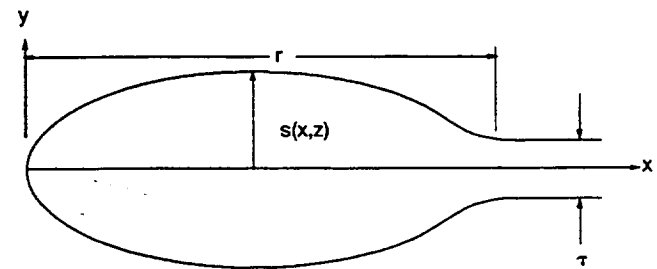


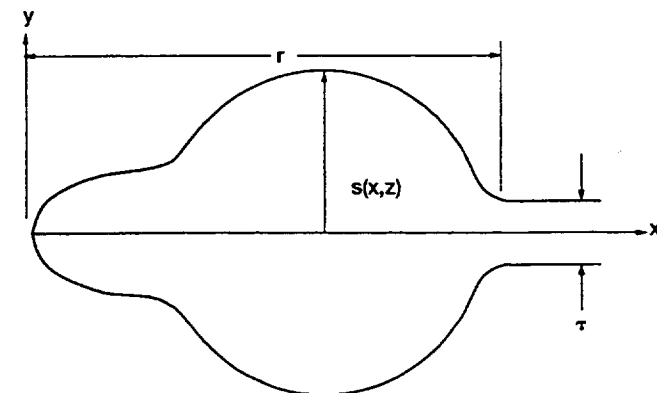
Figure 14.—Comparison of experimental and theoretical edge cross section dimensions.



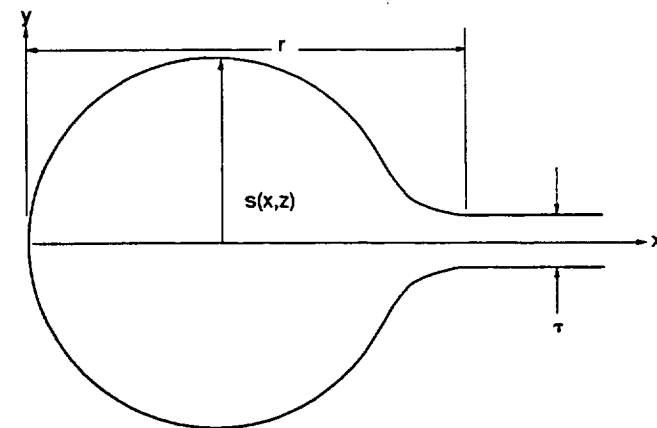
Initial, nearly circular cross-sectional shape



Flattened out or cigar like cross-sectional shape



Rebuilding or peanut like cross-sectional shape

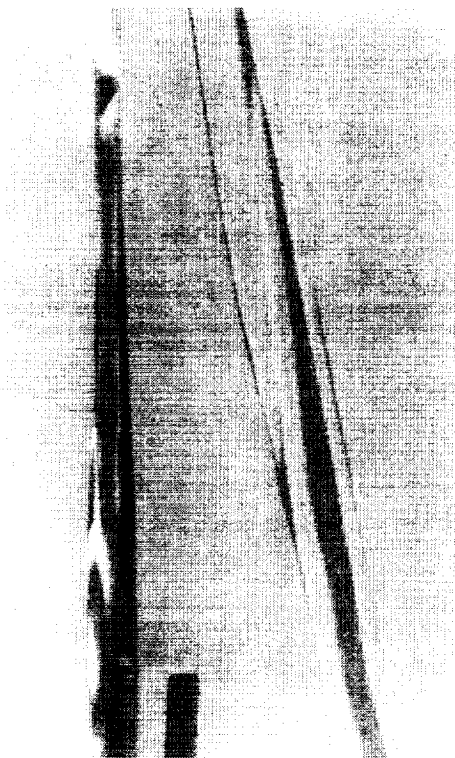


Larger, rebuilt, nearly circular cross-sectional shape

Figure 15.—Schematic of edge cross-section variation in flow direction.



(a) Edge cylinder at  $z = 1.5$  cm ( $z/L = 0.17$ ).



(b) Edge cylinder at  $z = 2.6$  cm ( $z/L = 0.29$ ).

Figure 16.—Photographs of plan edge views of sheet edge.  $W = 3.4$  cm,  $\tau = 100$   $\mu$ m,  $L = 8.9$  cm.



REPORT DOCUMENTATION PAGE			Form Approved OMB No. 0704-0188	
Public reporting burden for this collection of information is estimated to average 1 hour per response, including the time for reviewing instructions, searching existing data sources, gathering and maintaining the data needed, and completing and reviewing the collection of information. Send comments regarding this burden estimate or any other aspect of this collection of information, including suggestions for reducing this burden, to Washington Headquarters Services, Directorate for Information Operations and Reports, 1215 Jefferson Davis Highway, Suite 1204, Arlington, VA 22202-4302, and to the Office of Management and Budget, Paperwork Reduction Project (0704-0188), Washington, DC 20503.				
1. AGENCY USE ONLY (Leave blank)		2. REPORT DATE August 1993		3. REPORT TYPE AND DATES COVERED Technical Memorandum
4. TITLE AND SUBTITLE  A Study of Thin Liquid Sheet Flows			5. FUNDING NUMBERS  WU-506-41-11	
6. AUTHOR(S)  Donald L. Chubb, Frederick D. Calfo, Marc W. McConley, Matthew S. McMaster, and Abdollah A. Afjeh				
7. PERFORMING ORGANIZATION NAME(S) AND ADDRESS(ES)  National Aeronautics and Space Administration Lewis Research Center Cleveland, Ohio 44135-3191			8. PERFORMING ORGANIZATION REPORT NUMBER  E-7854-1	
9. SPONSORING/MONITORING AGENCY NAME(S) AND ADDRESS(ES)  National Aeronautics and Space Administration Washington, D.C. 20546-0001			10. SPONSORING/MONITORING AGENCY REPORT NUMBER  NASA TM-106323	
11. SUPPLEMENTARY NOTES Donald L. Chubb and Frederick D. Calfo, NASA Lewis Research Center; Marc W. McConley Princeton University, Princeton, New Jersey 08544; and Matthew S. McMaster and Abdollah A. Afjeh, University of Toledo, Toledo, Ohio 43606. Responsible person, Donald L. Chubb, (216) 433-2242.				
12a. DISTRIBUTION/AVAILABILITY STATEMENT  Unclassified - Unlimited Subject Categories 20 and 34			12b. DISTRIBUTION CODE	
13. ABSTRACT (Maximum 200 words)  This study was a theoretical and experimental investigation of thin liquid sheet flows in vacuum. A sheet flow created by a narrow slit of width, $W$ , coalesces to a point at a distance, $L$ , as a result of surface tension forces acting at the sheet edges. As the flow coalesces the fluid accumulates in the sheet edges. The observed triangular shape of the sheet agrees with the calculated triangular result. Experimental results for $L/W$ as a function of Weber number, $We$ , agree with the calculated result, $L/W = \sqrt{8We}$ . The edge cross sectional shape is found to oscillate from elliptic to "cigar" like to "peanut" like and then back to elliptic in the flow direction. A theoretical one-dimensional model was developed that yielded only elliptic solutions for the edge cross section. At the points where the elliptic shapes occur there is agreement between theory and experiment.				
14. SUBJECT TERMS  Thin film flow			15. NUMBER OF PAGES 28	
			16. PRICE CODE A03	
17. SECURITY CLASSIFICATION OF REPORT Unclassified	18. SECURITY CLASSIFICATION OF THIS PAGE Unclassified	19. SECURITY CLASSIFICATION OF ABSTRACT Unclassified	20. LIMITATION OF ABSTRACT	